Supporting Information

Temperature-dependent Raman study and determination of anisotropy ratio and in-plane thermal conductivity of low-temperature CVD grown $PdSe_2$ using unpolarized laser excitation

Tadasha Jena[1], Md Tarik Hossain[2], and P. K. Giri[1, 2*]

[1]*Centre for Nanotechnology, Indian Institute of Technology Guwahati, Guwahati - 781039, India*

[2]*Department of Physics, Indian Institute of Technology Guwahati, Guwahati - 781039, India*

[*] Corresponding author, email giri@iitg.ac.in (PKG)

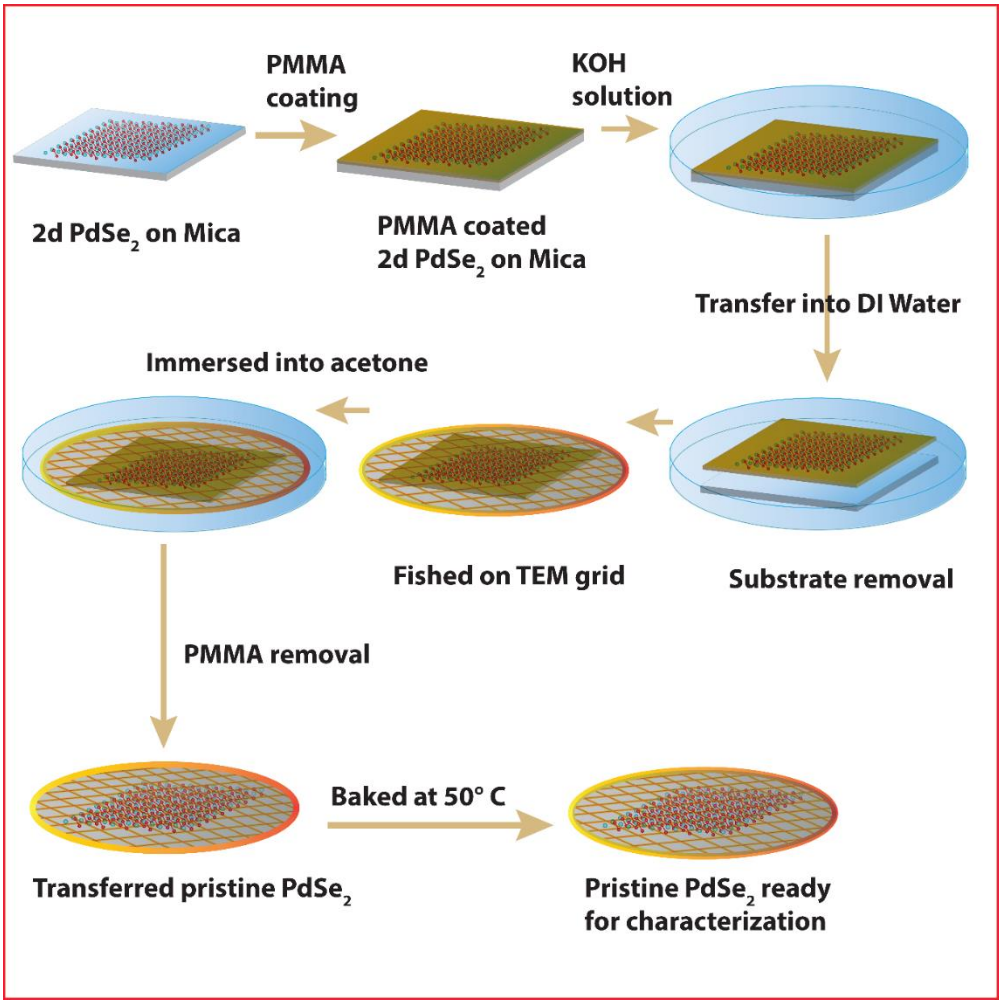

Fig. S1: Schematic of the transfer process of 2D $PdSe_2$ flakes from mica substrate to the target substrate.

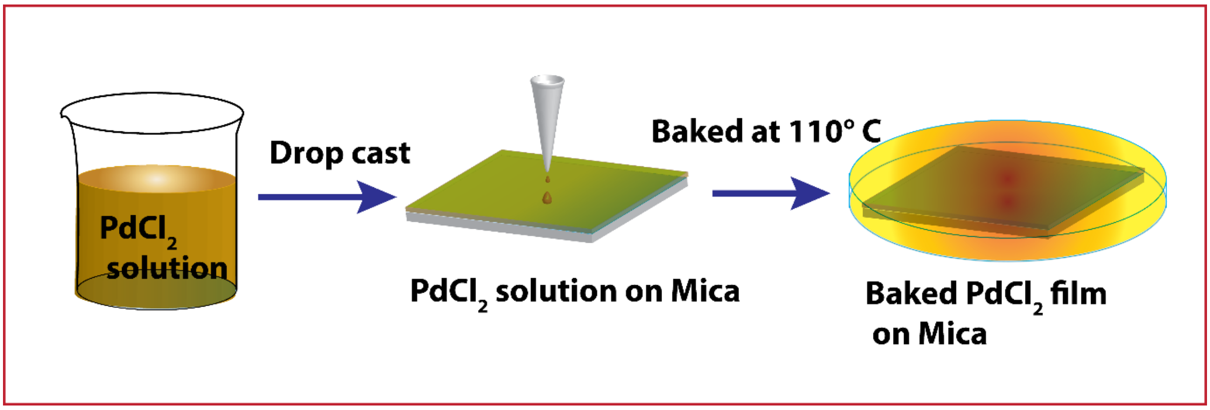

Fig. S2: Schematic representation of substrate preparation used for the growth of 2D $PdSe_2$ flakes.

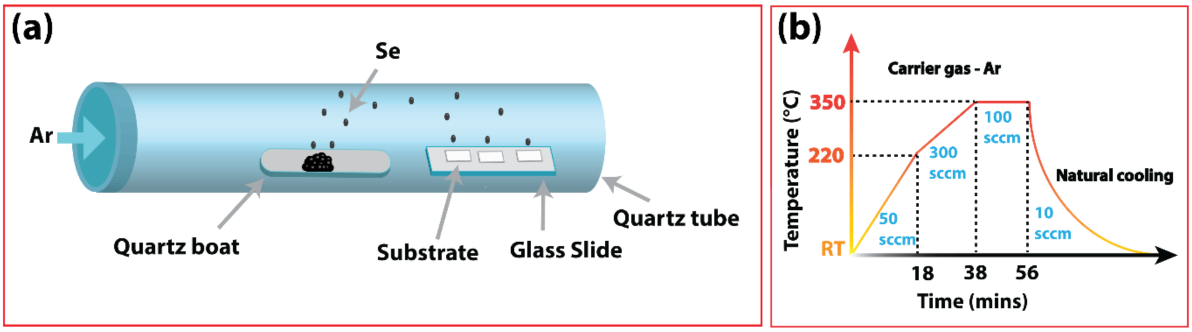

Fig. S3: (a) Schematic representation of the CVD setup used to grow 2D $PdSe_2$ flakes. (b) Temperature profile and growth parameters of CVD grown 2D $PdSe_2$.

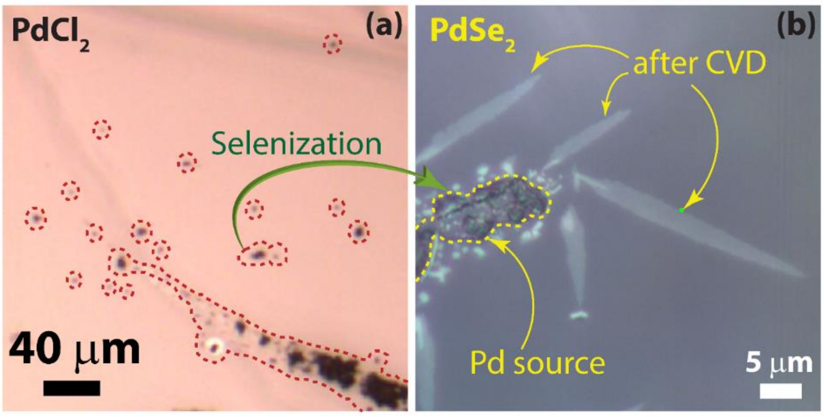

Fig. S4: (a) Inhomogeneous distribution of $PdCl_2$ solution on mica substrate after evaporation, which acts as a Pd source in the CVD process. (b) During the CVD, it follows a selenization process where ribbon-like and sheet-like $PdSe_2$ were formed after dragging Pd from Pd source.

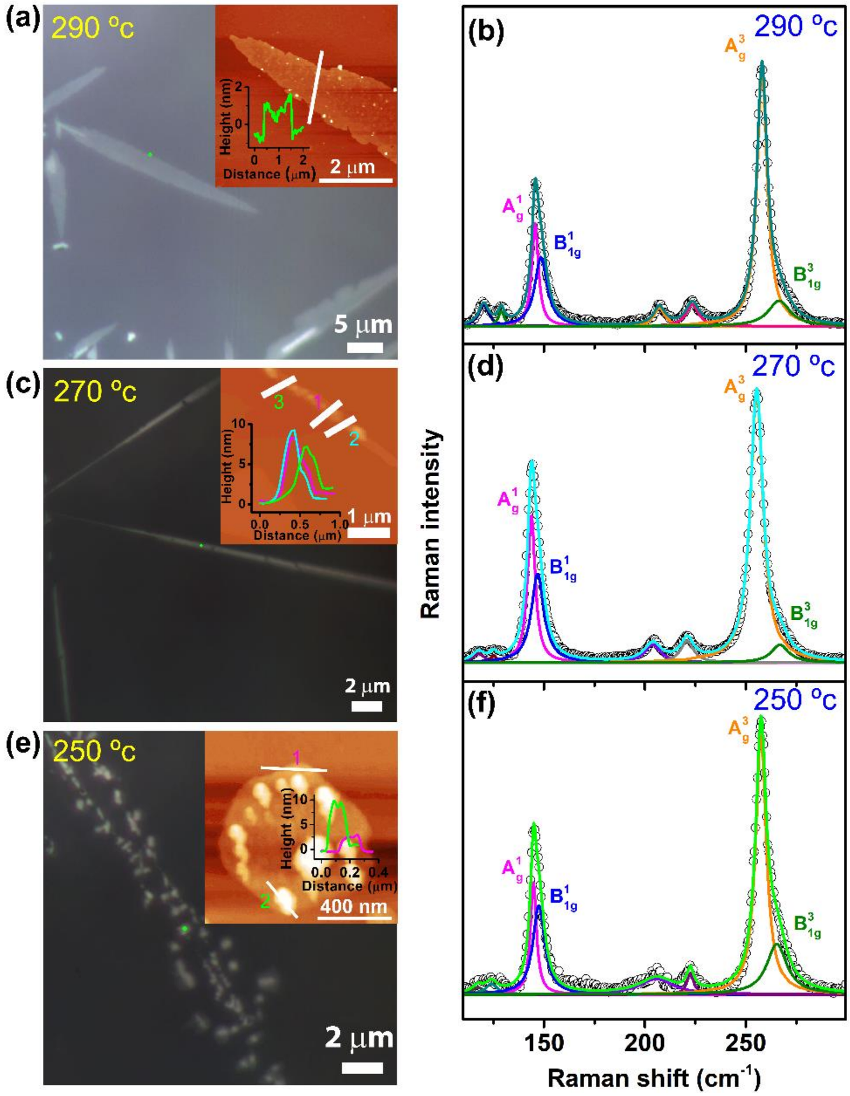

Fig. S5: Optical images of (a, c, e) layered $PdSe_2$ grown with substrate temperatures 290°C, 270°C, 250°C, respectively. The inset shows the corresponding AFM images with height profiles. (b, d, f) Corresponding Raman spectra of the samples (on mica substrate) for different growth temperatures.

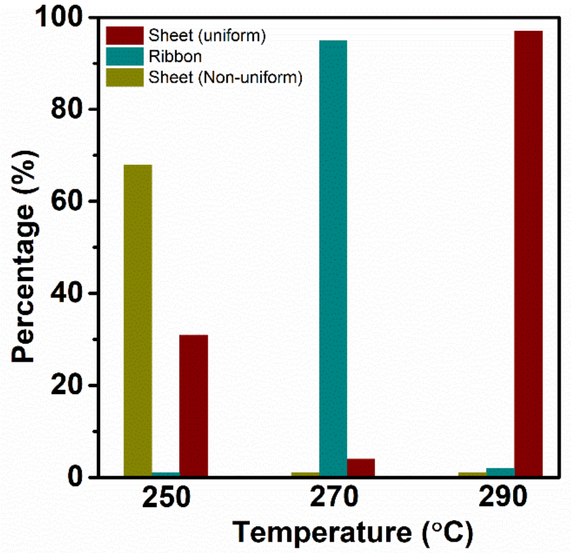

Fig. S6: Distribution percentage for three types of $PdSe_2$ (uniform sheet-like, ribbon-like, non-uniform sheet-like) structures observed at different growth temperatures 250°C, 270°C, 290°C.

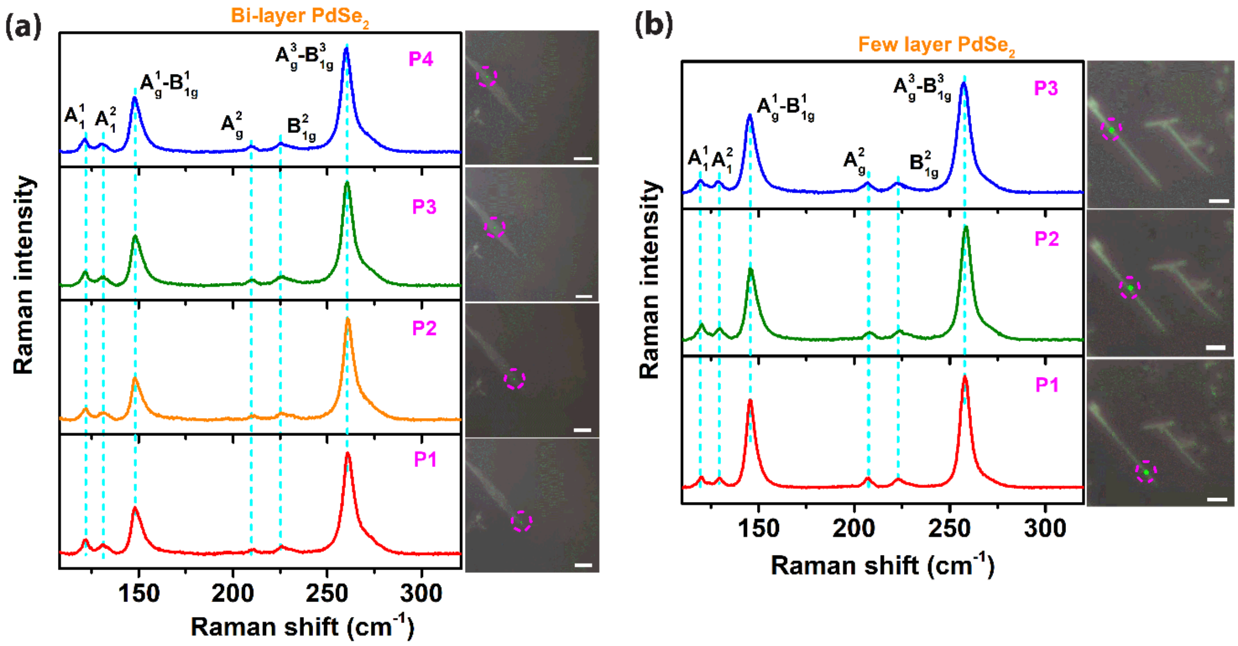

Fig. S7: Stacked Raman spectra at different locations on (a) bilayer $PdSe_2$ (b) few-layer $PdSe_2$ showing high uniformity of the layers. In the optical images, the scale bar is 5 μm for (a) and 2 μm for (b).

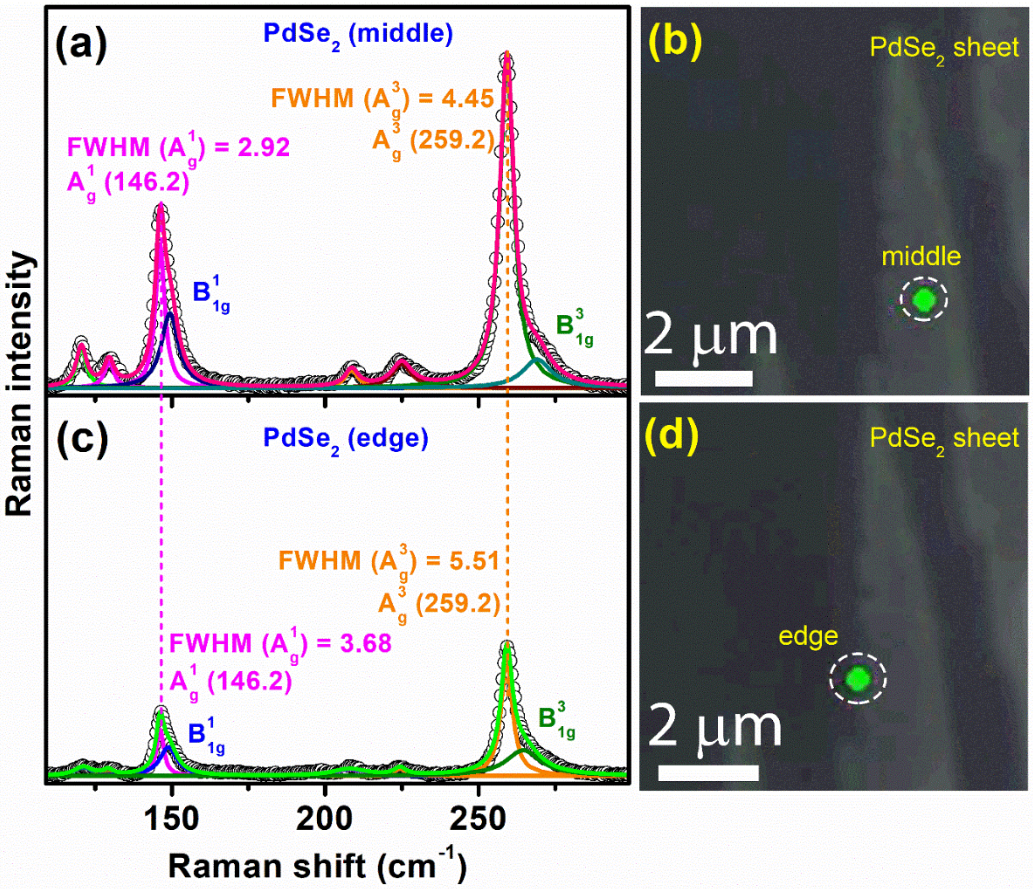

Fig. S8: (a) Raman spectra of the demarcated spot (middle) of $PdSe_2$ sheet, (b) the corresponding optical image. (c) Raman spectra of the demarcated spot (edge) of $PdSe_2$ sheet, (d) the corresponding optical image. Raman intensity for both the panels is same.

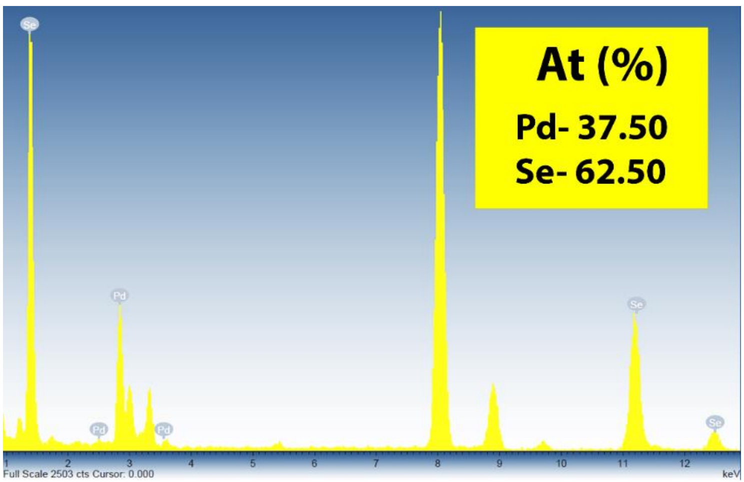

Fig. S9: EDX spectrum for CVD grown $PdSe_2$.

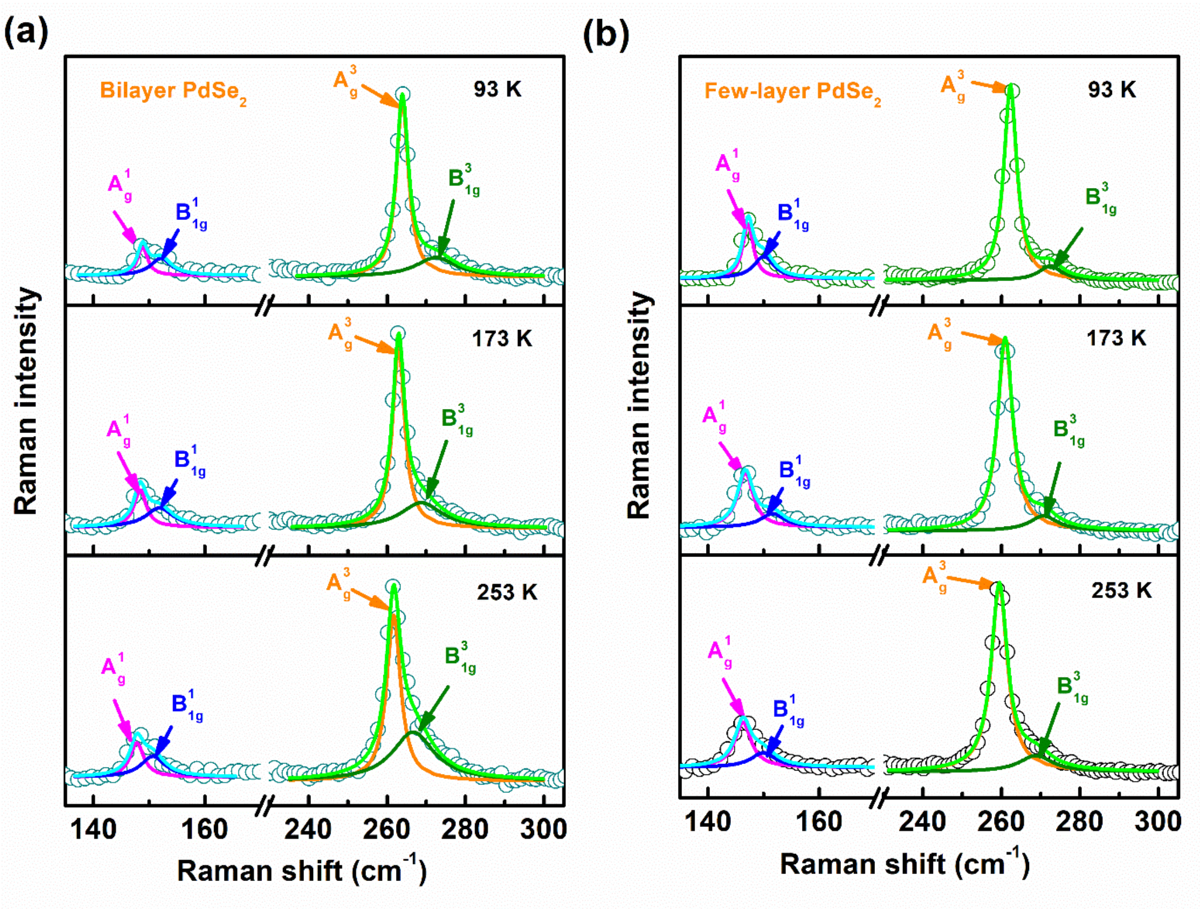

Fig. S10: Fitted low-temperature Raman spectra for (a) bi-layer and (b) few layer $PdSe_2$ for temperatures 93 K, 173 K, 253 K.

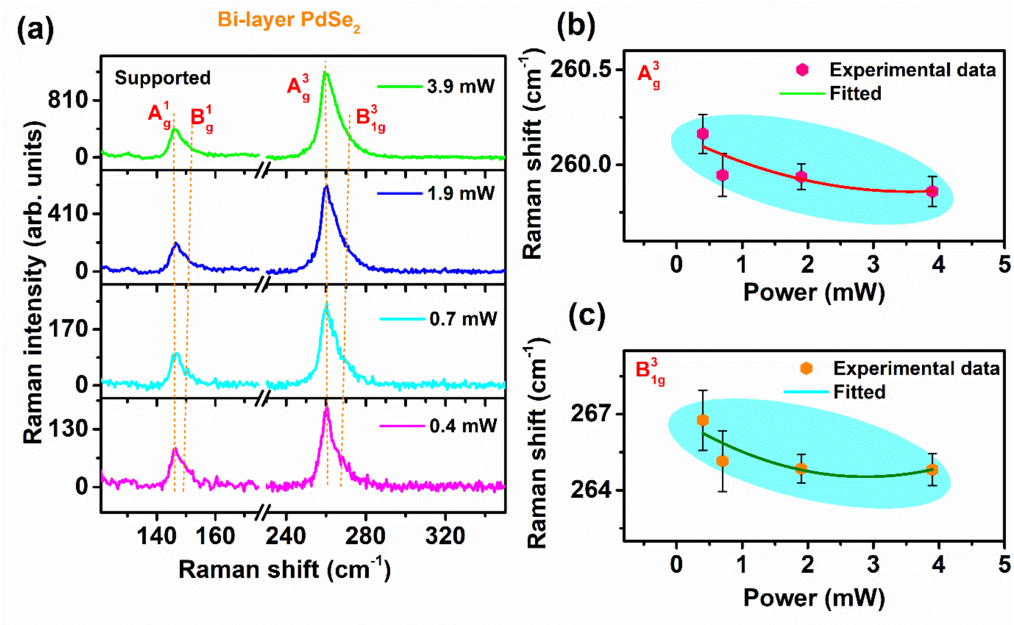

Fig. S11: (a) Power-dependent Raman spectra for bi-layer $PdSe_2$ in supported mode. (b,c) The corresponding Raman shift vs. power plot for A^3_g, and B^3_{1g} Raman modes, respectively. The symbols represent the experimental data, and the solid line refers to the fitted data using **equation S1**.

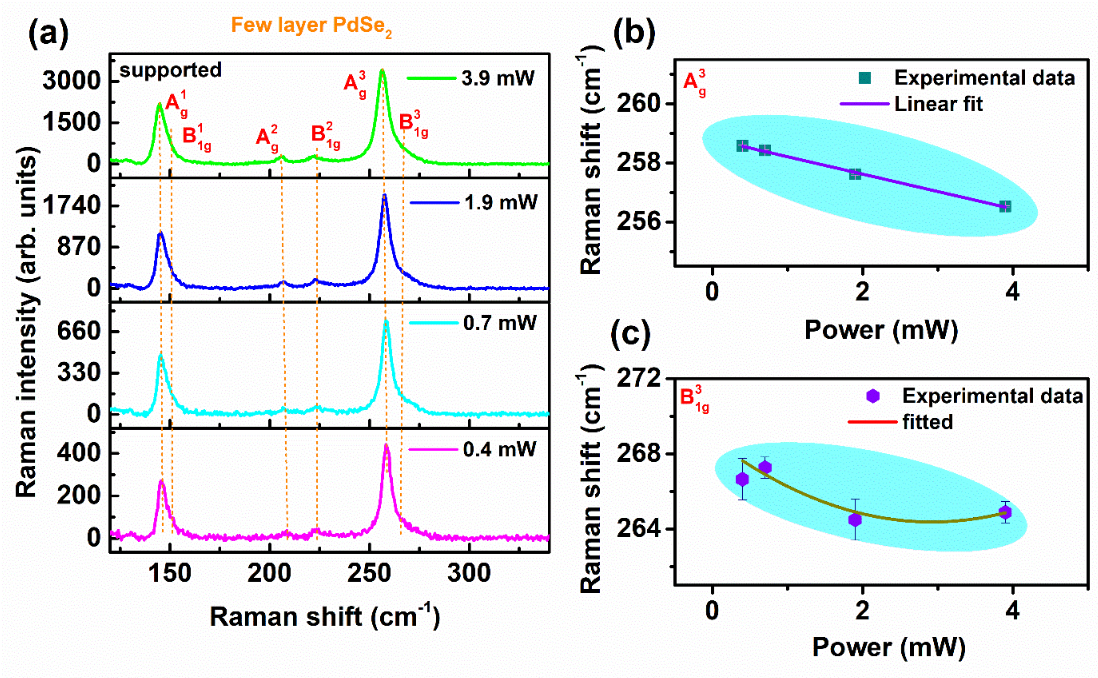

Fig. S12: (a) Power-dependent Raman spectra for few-layer $PdSe_2$ in supported mode. (b,c) The corresponding Raman shift vs. power for A^3_g, and B^3_{1g} Raman modes, respectively. The symbols represent the experimental data, and the solid line refers to the fitted data using **equation S1**.

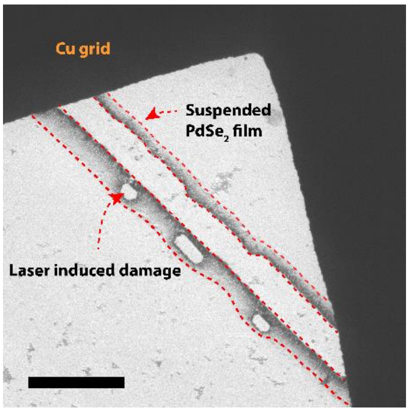

Fig. S13: Low-resolution TEM image of suspended flakes on Cu grid. The scale bar is 10 μm.

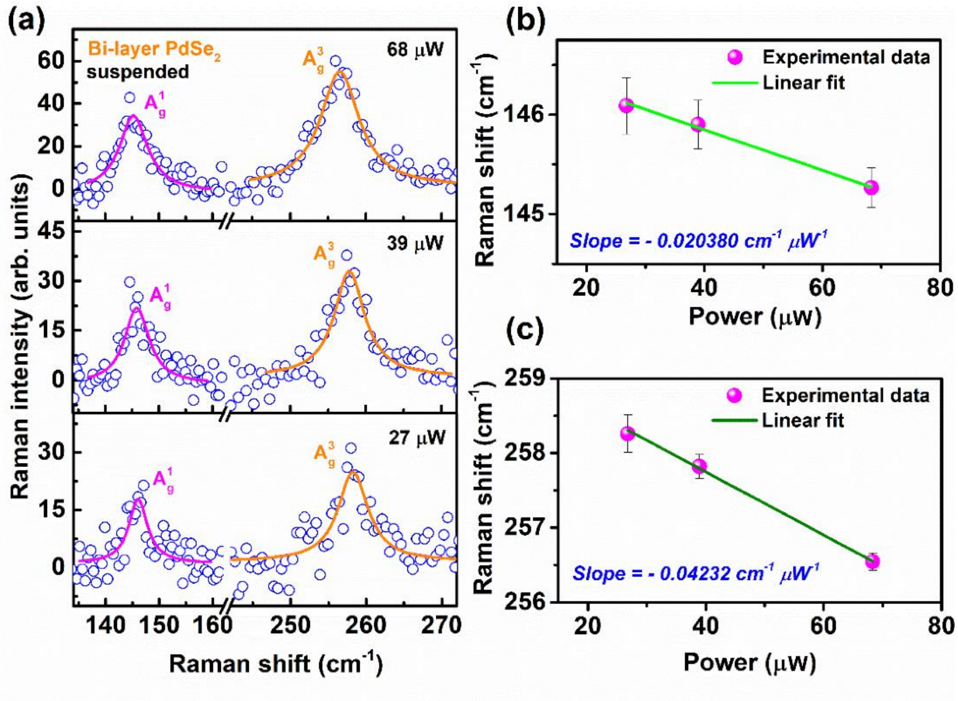

Fig. S14: (a) Laser power-dependent Raman spectra of suspended bi-layer $PdSe_2$. Corresponding Raman shift for (b) A_g^1 and (c) A_g^3 modes with laser power. Solid line indicates the linear fit.

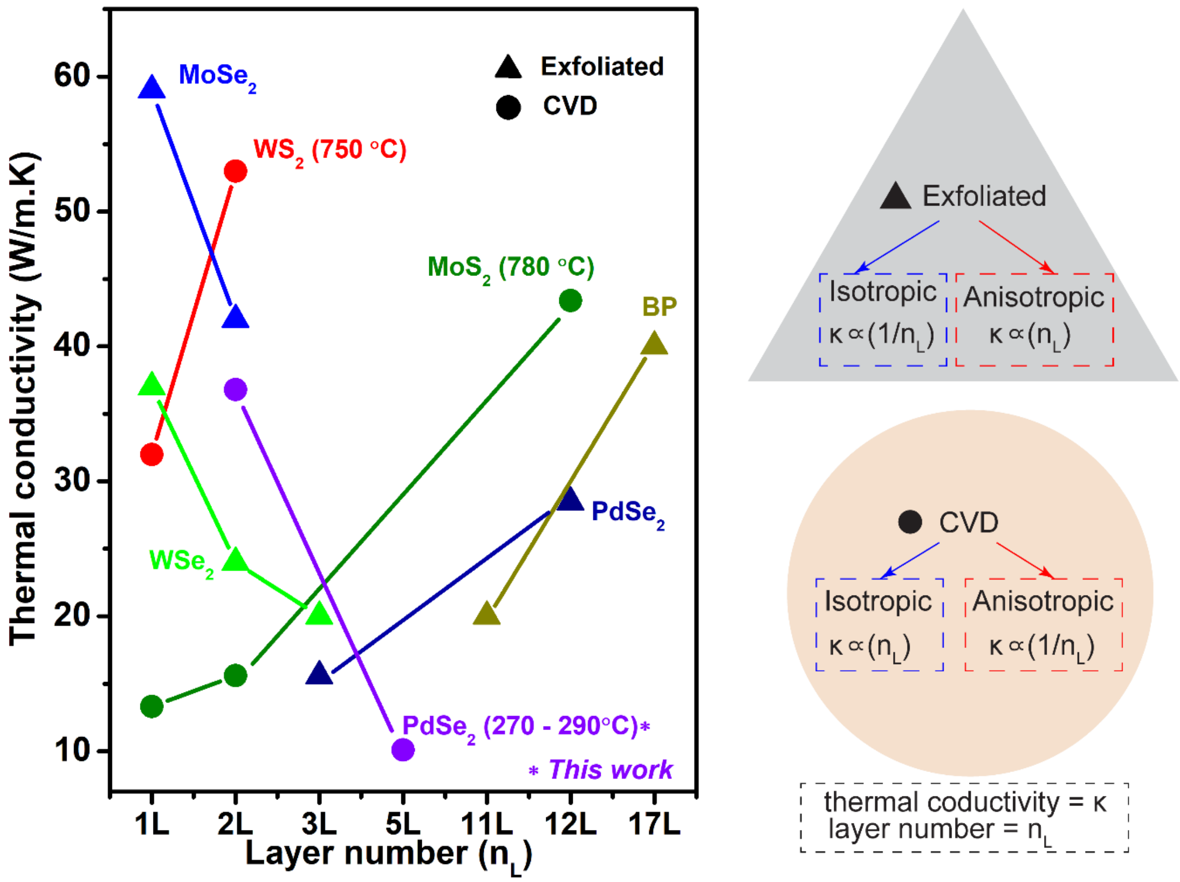

Fig. S15: Comparison of thermal conductivity of $PdSe_2$ with other conventional 2D materials for different layer numbers.[1-6]The schematic illustrations on the right side reflects the thermal conductivity relationship with layer number for CVD grown and exfoliated isotropic and anisotropic 2D materials.

Table S1: Relative spectral shifts of different Raman modes of CVD-grown bi-layer and few-layer $PdSe_2$.

Modes	Raman shift		Spectral downshift (cm^{-1})
	Bilayer $PdSe_2$ (cm^{-1})	Few layer $PdSe_2$ (cm^{-1})	
A^1_1	120.8	119.9	0.9
A^2_1	129.8	128.0	1.8
A^1_g	146.1	144.6	1.5
B^1_{1g}	150.5	147.5	3
A^2_g	207.9	205.6	2.3
B^2_{1g}	224.2	222.5	1.7
A^3_g	259.3	257.1	2
B^3_{1g}	268.2	268.5	-0.3

Table S2: Relative change in linewidths with change in layer number for different Raman modes of CVD grown $PdSe_2$.

Modes	FWHM		Relative change in FWHM for few layer $PdSe_2$
	Bilayer $PdSe_2$ (cm^{-1})	Few layer $PdSe_2$ (cm^{-1})	
A^1_1	5.43	7.74	increase
A^2_1	3.87	2.60	decrease
A^1_g	4.15	4.08	decrease
B^1_{1g}	5.43	7.16	increase
A^2_g	10.40	7.82	decrease
B^2_{1g}	4.75	7.22	increase
A^3_g	5.15	7.24	increase
B^3_{1g}	10.55	10.39	decrease

Table S3: Comparison of Raman peak position, FWHM of A_g^1 and A_g^3 mode in $PdSe_2$ at different growth temperatures.

Growth temperature	A^1_g (cm^{-1})	FWHM (cm^{-1})	A^3_g (cm^{-1})	FWHM (cm^{-1})
290 °C	145.6	3.99	258.1	6.2
270 °C	143.8	4.56	255.4	7.7
250 °C	144.8	3.8	257.5	6.3

Table S4: Fitting parameters of Raman spectra in figure 4 and 5.

Temperature (°C)	Bi-layer $PdSe_2$ (Raman shift)				Few-layer $PdSe_2$ (Raman shift)			
	A_g^1 mode (cm^{-1})	standard error	B_{1g}^1 mode (cm^{-1})	standard error	A_g^3 mode (cm^{-1})	standard error	B_{1g}^3 mode (cm^{-1})	standard error
93	147.19	0.09	150.22	0.74	262.26	0.02	272.52	0.45
113	147.39	0.10	151.28	0.72	262.15	0.03	272.82	0.39
133	146.82	0.11	149.84	0.85	261.67	0.02	271.66	0.39
153	146.74	0.11	149.53	0.75	261.50	0.02	270.35	0.60
173	146.64	0.09	152.18	0.82	260.91	0.03	270.84	0.48
193	146.95	0.12	150.84	1.02	260.91	0.02	269.24	0.46
213	146.82	0.10	150.77	1.33	260.50	0.02	270.63	0.40
223	146.72	0.11	150.70	1.17	260.53	0.02	270.67	0.55
243	146.16	0.09	149.26	0.75	259.84	0.03	268.84	1.00
263	145.86	0.29	148.93	1.01	259.16	0.03	268.73	0.68

Excitation Power dependent Raman study (supported $PdSe_2$ flakes):

Power-dependent micro-Raman measurement was carried out to understand the localized heating effect on Raman modes of CVD grown $PdSe_2$. **Fig. S13(a)** shows the stacked Raman spectra of a bilayer $PdSe_2$ film in a particular position. Here Raman measurement is carried out on pristine $PdSe_2$ film grown on mica substrate (supported state). An apparent spectral redshift in Raman modes is discerned whenever excitation power increases. We varied the effective power from 0.4 mW to 3.9 mW by varying ND filters equipped with the instrument. Note that, even in higher power than the power used in suspended condition, we did not observe the sample damage. To better understand the origin of spectral shift, we further fitted all spectrum with Lorentzian lineshape. The spectral shift is observed due to the anharmonicity in the system generated due to localized heating. **Fig. S13(b,c)** shows the corresponding extracted Raman shift vs. Power plot for A^3_g, B^3_{1g} mode, respectively. We observed a non-linear spectral redshift for both modes in the bilayer. The non-linear variation may be due to the quicker heat dissipation to the supported substrate. The non-linear behavior has been fitted with the equation

$$w(P) = w_0 + \beta P + \gamma P^2 \ , \qquad \textbf{(S1)}$$

where β and γ are constants. The second and third term corresponds to power generated localized heating effect and thermal expansion effect. For bilayer β and γ are - 0.16 and 0.023 in A^3_g mode -1.61 and 0.28 in B^3_{1g} mode. Similarly, Raman spectra for few-layer are recorded in different laser powers. **Fig. S14(a)** shows stacked Raman spectra of few-layer $PdSe_2$ within the power of 0.4 mW to 3.9 mW. **Fig. S14(b, c)** shows the corresponding spectral shift in A^3_g, B^3_{1g} with power variation for few-layer $PdSe_2$. Unlike bilayer $PdSe_2$, in few-layer $PdSe_2$, a linear shift in A^3_g but non-linear B^3_g mode was observed. A^3_g mode gives a linear slope value -0.5 $cm^{-1}mW^{-1}$. The obtained β and γ values are -2.99 and 0.51 in B^3_g mode for few-layer $PdSe_2$. To avoid the substrate effect and related error in calculation, we transferred the sample on a Cu grid to measure the purely power dependent effect on $PdSe_2$.

References:

1. Luo, Z., et al., *Anisotropic in-plane thermal conductivity observed in few-layer black phosphorus.* Nature Communications, 2015. **6**(1): p. 8572.

2. Zhang, X., et al., *Measurement of Lateral and Interfacial Thermal Conductivity of Single- and Bilayer MoS2 and MoSe2 Using Refined Optothermal Raman Technique.* ACS Applied Materials & Interfaces, 2015. **7**(46): p. 25923-25929.
3. Easy, E., et al., *Experimental and Computational Investigation of Layer-Dependent Thermal Conductivities and Interfacial Thermal Conductance of One- to Three-Layer WSe2.* ACS Applied Materials & Interfaces, 2021. **13**(11): p. 13063-13071.
4. Peimyoo, N., et al., *Thermal conductivity determination of suspended mono- and bilayer WS2 by Raman spectroscopy.* Nano Research, 2015. **8**(4): p. 1210-1221.
5. Chen, L., et al., *In-Plane Anisotropic Thermal Conductivity of Low-Symmetry PdSe2.* Sustainability, 2021. **13**(8).
6. Bae, J.J., et al., *Thickness-dependent in-plane thermal conductivity of suspended MoS2 grown by chemical vapor deposition.* Nanoscale, 2017. **9**(7): p. 2541-2547.